# Creating Order from Random Fluctuations in Small Spin Ensembles

R. Budakian, *et al.*

*Science* **307**, 408 (2005);
DOI: 10.1126/science.1106718

# Creating Order from Random Fluctuations in Small Spin Ensembles

R. Budakian,* H. J. Mamin, B. W. Chui, D. Rugar

We demonstrate the ability to create spin order by using a magnetic resonance force microscope to harness the naturally occurring statistical fluctuations in small ensembles of electron spins. In one method, we hyperpolarized the spin system by selectively capturing the transient spin order created by the statistical fluctuations. In a second method, we took a more active approach and rectified the spin fluctuations by applying real-time feedback to the entire spin ensemble. The created spin order can be stored in the laboratory frame for a period on the order of the longitudinal relaxation time of 30 seconds and then read out.

Creating order from random thermal fluctuations has been of interest to physicists since the development of statistical mechanics in the 19th century (*1*). In a more modern context, creating order in microscopic physical systems is an essential part of quantum information processing and quantum computation (*2*–*4*), where the ability to set the state of a collection of quantum objects to a desired configuration is required. The device used to perform this operation must be capable of controlling the microscopic degrees of freedom of the system while being subjected to environmental fluctuations.

Here, we take advantage of the outstanding sensitivity of magnetic resonance force microscopy (MRFM) to follow statistical $\sqrt{N}$ fluctuations in small ensembles of electron spins (*5*, *6*) with a real-time sensitivity corresponding to $1.3\mu_B$, where $\mu_B$ is the Bohr magneton. The spin manipulation protocols we have developed allow us to monitor and respond to the instantaneous spin imbalance in the rotating frame. By monitoring the spin system and selectively capturing the large positive fluctuations, we have created a mean polarization corresponding to $\sim 6\mu_B$ in an ensemble of $N \approx 70$ spins. We also used real-time feedback to effectively cool the spin system and create a mean polarization corresponding to $\sim 7\mu_B$. The spin order was then transferred to the laboratory frame, stored, and later read out.

In MRFM detection, spins are manipulated by using magnetic resonance, and the longitudinal component of the magnetization is detected mechanically by measuring the interaction between the spins and a small permanent magnet attached to the end of a sensitive silicon cantilever. Typically, the force generated by a spin on the cantilever is quite small. An electron spin will produce a force of only $2 \times 10^{-18}$ N when subjected to a magnetic field gradient from the tip as large as $2 \times 10^5$ T m$^{-1}$. Sensitivity to such small forces requires the ability to coherently manipulate spins for many cycles of the cantilever. Recently, through the use of specially engineered cantilevers that reduce disturbance to the spins (*7*–*9*), we observed longitudinal relaxation times in the rotating frame (i.e., during measurement) of up to several seconds. This has allowed us to realize a single-shot detection sensitivity approaching the single spin level (*5*) and the detection of an isolated electron spin by signal averaging (*6*).

In the experimental setup of the MRFM apparatus (Fig. 1A), a custom-fabricated mass-loaded silicon cantilever with a submicrometer SmCo magnetic particle attached to the tip is used as the force-sensing element (*5*, *6*). The sample consists of vitreous silica (Suprasil W2, Heraeus Quarzglas GmbH and Company KG, Hanau, Germany) that has been irradiated by gamma rays from a $^{60}$Co source to produce spin-1/2 paramagnetic defects or $E'$ centers (unpaired electron spins on Si) (*10*). Experiments were performed with two different cantilever and sample combinations. In setup 1, a cantilever having a fundamental resonance frequency $f_c = 8.7$ kHz and stiffness $k = 0.6$ mN m$^{-1}$ with a 250-nm-wide SmCo tip was used with a sample that had a spin concentration of $\sim 10^{15}$ cm$^{-3}$. In setup 2, a cantilever with $f_c = 5.5$ kHz, $k = 0.11$ mN m$^{-1}$, and a 150-nm-wide SmCo tip was used with a $\sim 10^{14}$ cm$^{-3}$ concentration sample. The MRFM apparatus was operated in vacuum and cooled to 300 mK to reduce the thermal vibrations of the cantilever.

Electron spin resonance was excited at $\omega_{rf}/2\pi = 2.96$ GHz with the use of a microwave field with amplitude $B_1 \approx 0.3$ mT. In the presence of the inhomogeneous field from the tip, only those spins within a thin resonant slice satisfying the resonance condition given by $B_0(x,y,z) \equiv |\mathbf{B}_{tip}(x,y,z) + B_{ext}\hat{\mathbf{z}}| = \omega_{rf}/\gamma$ will interact with the microwave field. Here, $B_0(x, y, z)$ is the sum of the tip field, $\mathbf{B}_{tip}(x, y, z)$, and a uniform external field, $B_{ext}\hat{\mathbf{z}}$, produced by a superconducting magnet, and $\gamma$ is the gyromagnetic ratio ($\gamma/2\pi = 2.8 \times 10^{10}$ Hz T$^{-1}$). For the vertical orientation of the cantilever shown in Fig. 1A, only those spins that are slightly to the left or right of the tip contribute to the signal. Furthermore, because of symmetry, the cantilever will respond only to the left-right imbalance of spin polarization.

To detect spins, we use the recently developed spin manipulation protocol OSCAR (oscillating cantilever-driven adiabatic reversal), which measures the shift in the fundamental frequency of the cantilever in response to tip-spin interactions (*5*, *6*, *11*). The cantilever is self-oscillated at its fundamental resonance frequency by using a piezoelectric transducer that drives the cantilever to a fixed amplitude $x_{pk}$ (*11*, *12*). As the cantilever position oscillates according to $x_c(t) =$

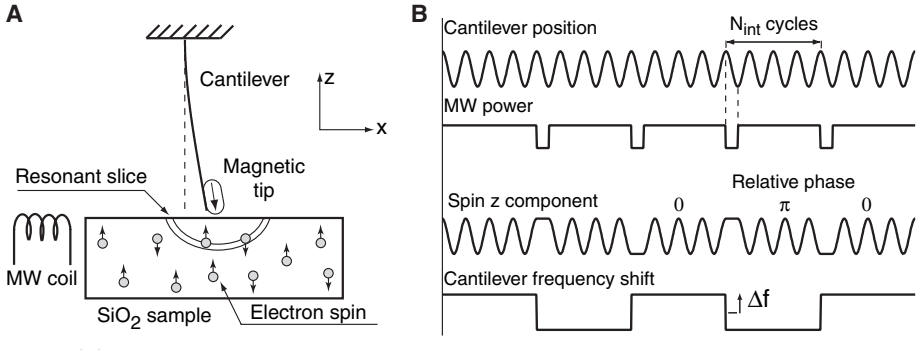


**Fig. 1.** (**A**) Schematic of the MRFM apparatus. The cantilever with the attached magnetic tip is oriented vertically about 140 nm away from the surface of a sample containing a low concentration of $E'$ centers. A small coil placed near the sample generates microwaves at 2.96 GHz to excite electron spin resonance. At 2.96 GHz, the resonance condition for electrons is met for $B_0 = 106$ mT. For $B_{ext} = 30$ mT, the resonant slice is a paraboloidal shell that extends about 250 nm below the tip. (**B**) Timing diagram for the interrupted OSCAR protocol. For setups 1 and 2, the microwave (MW) power is interrupted every 88 cycles ($f_{sig} \approx 50$ Hz) and 64 cycles ($f_{sig} \approx 43$ Hz), respectively.

IBM Research Division, Almaden Research Center, 650 Harry Road, San Jose, CA 95120, USA.

*To whom correspondence should be addressed. E-mail: budakian@us.ibm.com

$x_{pk}\sin(2\pi f_c t)$, the field experienced by a spin near the tip is modulated sinusoidally at the cantilever frequency with peak amplitude $\Delta B = Gx_{pk}$, where $G = \partial B_0/\partial x$ is the lateral gradient from the tip. For typical experimental parameters of $x_{pk} \approx 20$ nm and $G \approx 2 \times 10^5$ T m$^{-1}$, the external field experienced by spins within the resonant slice is modulated by $\Delta B = 4$ mT. In the presence of the microwave field, the slow variation of the static field at the cantilever frequency causes each spin within the resonant slice to be adiabatically inverted synchronously with the cantilever motion. The back action of the spin on the cantilever in turn shifts the fundamental frequency of the cantilever by a small amount

$$\delta f_i = \frac{2 f_c G_i \mu_B}{\pi k x_{pk}} \alpha_i$$

where $G_i$ is the gradient at the position of the $i$th spin and $\alpha_i$ is a random variable that takes values +1 or –1, depending on whether the spin moment is aligned or anti-aligned with respect to the effective field in the rotating frame (*5*, *13*, *14*). The two-level nature of $\alpha_i$ reflects the quantum measurement characteristic of MRFM spin detection (i.e., a rotating frame Stern-Gerlach behavior) (*15*–*17*). For an ensemble of $N$ spins, we define the instantaneous statistical spin imbalance in the rotating frame to be $\Delta N = \sum_{i=1}^{N} \alpha_i$ and the corresponding magnetic moment to be $\Delta m = \Delta N \mu_B$. The cantilever frequency shift for the ensemble is given by $\Delta f = \sum_{i=1}^{N} \delta f_i$.

Near the surface of the sample, the cantilever frequency is affected not only by the presence of the spins but also by the more dominant electrostatic and van der Waals forces. In order to make the spin component of the signal distinctive, we periodically reversed the sign of the frequency shift by interrupting the microwave power for 1/2 cycle of the cantilever vibration every $N_{int}$ cycles (Fig. 1B). The periodic interruptions encode the spin signal with a characteristic frequency $f_{sig} = f_c/2N_{int}$. A lock-in amplifier referenced to $f_{sig}$ is used to demodulate the frequency shift and determine $\Delta f$ (*5*, *6*).

A 200-s record of the cantilever frequency shift, recorded from the in-phase channel of the lock-in amplifier, is shown (Fig. 2A). A histogram of the frequency fluctuations (Fig. 2B) reveals a Gaussian shape with variance $\sigma_I^2 = 69$ mHz$^2$. We note that the distribution has a zero mean, indicating that the spin ensemble does not have a preferred direction with respect to the effective field. To show that the measured frequency shift is dominated by the spin signal rather than measurement noise, we show the histogram of the measurement noise recorded from the quadrature channel of the lock-in amplifier ($\sigma_Q^2 = 5$ mHz$^2$) (Fig. 2C). The variance of the spin signal without measurement noise is simply related to the in-phase and quadrature variances by $\sigma_{spin}^2 = \sigma_I^2 - \sigma_Q^2$ (*6*). From the measured variance $\sigma_{spin}^2$ and a model of the field produced by the tip (*18*), we estimate the total number of spins contained within the resonant slice to be $N \approx 70$.

The power spectrum of the frequency fluctuations (Fig. 2D) fits well to a Lorentzian with spectral width $\Delta\nu_s = 21$ mHz, corresponding to a correlation time $\tau_m = 1/2\pi\Delta\nu_s = 7.6$ s. This long correlation time, closely related to the rotating frame longitudinal relaxation time, allows us to measure real-time fluctuations of the spin ensemble with a lock-in time constant of up to 3 s.

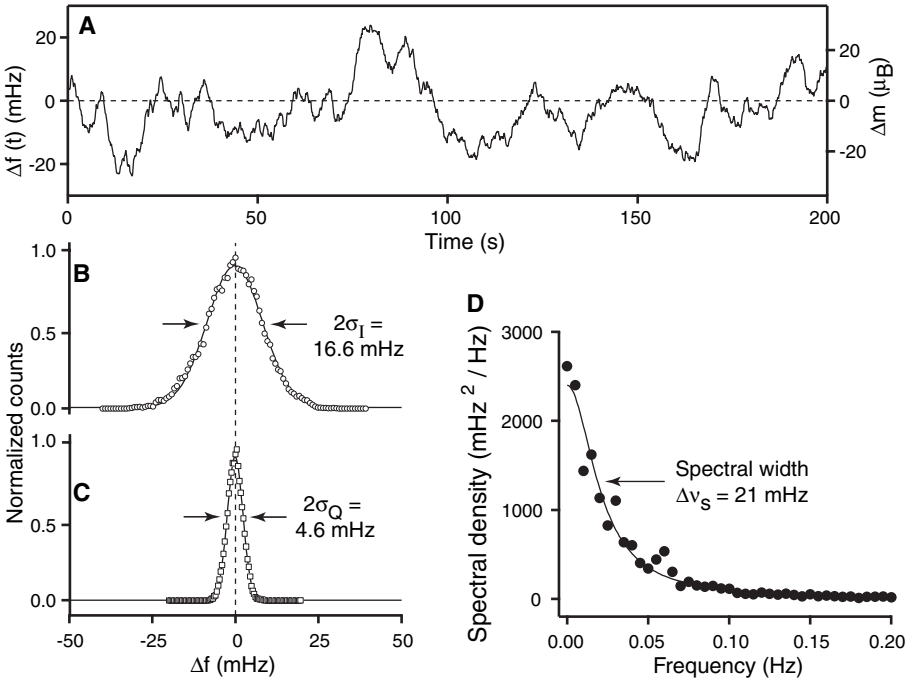


**Fig. 2.** (**A**) Trace showing a time record of the statistical fluctuations recorded in a 83-mHz bandwidth with the use of setup 1. The frequency shift is converted to equivalent number of spins (right-hand axis) by dividing $\Delta f$ by the average frequency shift per spin ($|\overline{\delta f}| = 0.8$ mHz/spin). (**B**) Histogram of a 1-hour continuous record of the in-phase lock-in output signal. The Gaussian distributed spin fluctuations have a zero mean, indicating that the time-averaged spin imbalance does not point in a preferred direction with respect to the effective field. This observation is consistent with the fact that the spin temperature in the rotating frame approaches $T_s = \infty$ for measurement times $t_{meas} \gg \tau_m$. (**C**) Histogram of the quadrature channel showing the detection noise. (**D**) Power spectrum of a 1-hour record of the fluctuations.

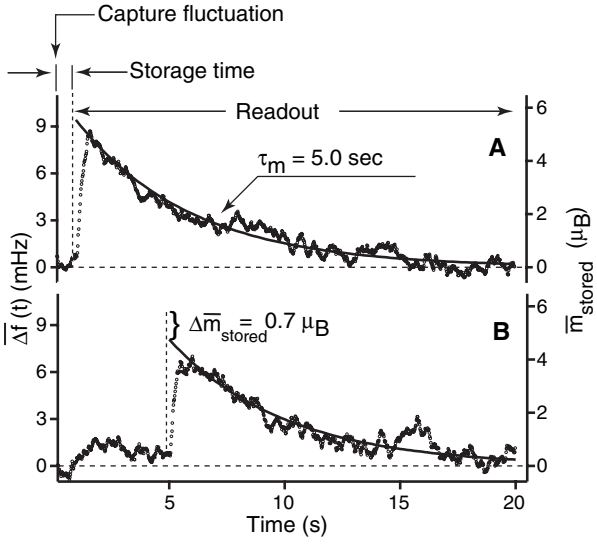


**Fig. 3.** (**A**) Trace showing the average of 2800 individual capture-store-readout sequences with a storage time of 1.0 s, taken with use of setup 2. The average frequency shift, $\overline{\Delta f}(t)$, and stored magnetization, $\overline{m}_{stored}$, are shown on the left- and right-hand axes, respectively. Equivalent spins are calculated by using $|\overline{\delta f}| = 1.7$ mHz/spin. (**B**) Data taken under the same conditions as (A), except the storage time was increased to 5.0 s. The decaying magnetization observed during readout in (A) and (B) fits well to an exponential indicating a $\tau_m = 5.0$ s spin relaxation time during measurement.

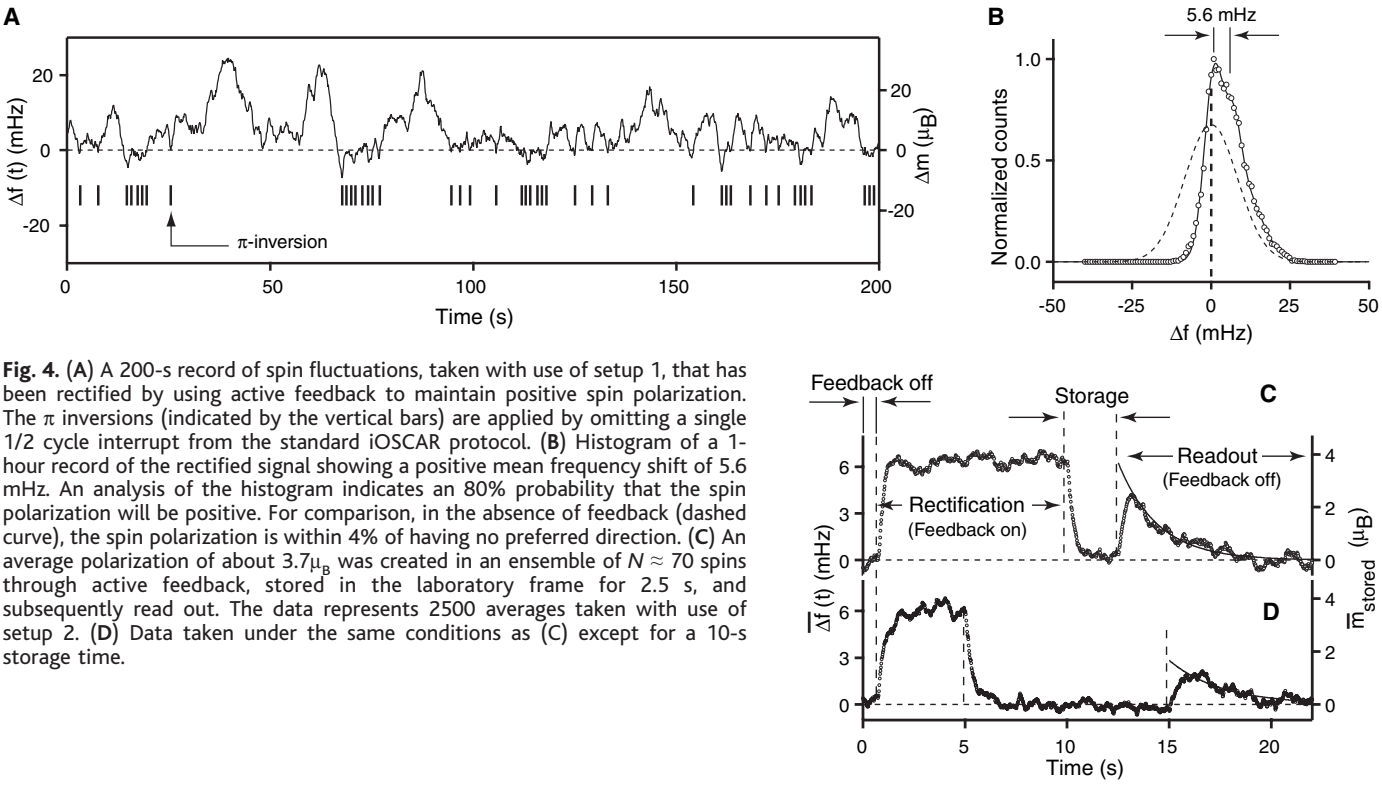


**Fig. 4.** (**A**) A 200-s record of spin fluctuations, taken with use of setup 1, that has been rectified by using active feedback to maintain positive spin polarization. The π inversions (indicated by the vertical bars) are applied by omitting a single 1/2 cycle interrupt from the standard iOSCAR protocol. (**B**) Histogram of a 1-hour record of the rectified signal showing a positive mean frequency shift of 5.6 mHz. An analysis of the histogram indicates an 80% probability that the spin polarization will be positive. For comparison, in the absence of feedback (dashed curve), the spin polarization is within 4% of having no preferred direction. (**C**) An average polarization of about $3.7\mu_B$ was created in an ensemble of $N \approx 70$ spins through active feedback, stored in the laboratory frame for 2.5 s, and subsequently read out. The data represents 2500 averages taken with use of setup 2. (**D**) Data taken under the same conditions as (C) except for a 10-s storage time.

As an initial demonstration of harnessing spin fluctuations, we created a hyperpolarized spin state by selectively capturing and storing the especially large statistical fluctuations. To do this, we continuously monitor the spin signal and wait until a fluctuation exceeds a predetermined threshold value $\Delta f_{threshold}$ (*19*). Upon registering a suitable fluctuation, the microwave power is turned off at a maximum of the cantilever motion, which leaves the instantaneous spin polarization pointing along $\mathbf{B}_0$. In the absence of the microwave field, the spins no longer respond to the cantilever motion, and the nonequilibrium state of the spin ensemble can be stored in the laboratory frame for as long as a spin-lattice relaxation time, $T_1$. The stored magnetization can then be read out by reapplying the microwave field at a maximum of the cantilever motion and using the standard interrupted OSCAR (iOSCAR) protocol.

The average of 2800 individual capture-store-readout sequences, taken with use of setup 2, is shown (Fig. 3). For the data in Fig. 3A, the captured magnetization was stored for 1 s in the laboratory frame (i.e., with the microwave field off) and then read out with use of the iOSCAR protocol. The readout signal had a peak amplitude of 9.4 mHz, which we estimate corresponds to an average magnetization of $\overline{m}_{stored} = 5.5\mu_B$. When the storage time was increased to 5 s (Fig. 3B), the peak stored magnetization decreased by 14% to $\overline{m}_{stored} = 4.8\mu_B$. This drop in $\overline{m}_{stored}$ is the result of depolarization due to longitudinal relaxation, indicating $T_1 \sim 30$ s. The observed $T_1$ includes the contribution from the lattice as well as tip-induced relaxation (*11*).

In addition to simply selecting and capturing desired fluctuations, we can also take a more active approach by applying real-time feedback to the spin system in order to continuously guide its evolution. As a demonstration of feedback control, we have rectified the spin fluctuations by monitoring the spin signal and applying a π inversion to the entire spin ensemble whenever $\Delta f < 0$ (*19*). The π inversions, accomplished with the use of adiabatic inversion, flip the sign of the spin imbalance so as to always keep $\Delta m$ positive in the iOSCAR reference frame. Figure 4A shows a 200-s record of the iOSCAR signal, taken with the use of setup 1, along with vertical bars indicating times when π inversions were applied. In contrast to Fig. 2B, the histogram of the signal with feedback control (Fig. 4B, solid curve) now shows a nonzero mean value of 5.6 mHz corresponding to $\sim 7.0\mu_B$. Thus, through the use of feedback, we have essentially hyperpolarized the spins in the rotating frame of the iOSCAR measurement. This spin order can once again be transferred to the laboratory frame, stored, and then read out (Fig. 4, C and D).

We have demonstrated real-time control of electron spins in small ensembles using two spin manipulation protocols: fluctuation capture and fluctuation rectification. Because the present single-shot detection sensitivity is already approaching the single spin level, relatively modest improvements in detection signal-to-noise ratio should allow real-time quantum state detection and control of individual electron spins.

### References and Notes


1. J. C. Maxwell, *Theory of Heat* (Longmans, London, ed. 6, 1880).
2. D. P. Divincenzo, *Science* **270**, 255 (1995).
3. B. E. Kane, *Nature* **393**, 133 (1998).
4. A. Steane, *Rep. Prog. Phys.* **61**, 117 (1998).
5. H. J. Mamin, R. Budakian, B. W. Chui, D. Rugar, *Phys. Rev. Lett.* **91**, 207604 (2003).
6. D. Rugar, R. Budakian, H. J. Mamin, B. W. Chui, *Nature* **430**, 329 (2004).
7. G. P. Berman, V. N. Gorshkov, D. Rugar, V. I. Tsifrinovich, *Phys. Rev. B* **68**, 094402 (2003).
8. B. W. Chui *et al.*, in *Technical Digest of the 12th International Conference on Solid-State Sensors and Actuators (Transducers '03)*, IEEE, Boston, MA, 8 to 12 June 2003 (IEEE, Piscataway, NJ, 2003), pp. 1120–1123.
9. D. Mozyrsky, I. Martin, D. Pelekhov, P. C. Hammel, *Appl. Phys. Lett.* **82**, 1278 (2003).
10. J. G. Castle, D. W. Feldman, P. G. Klemens, R. A. Weeks, *Phys. Rev.* **130**, 577 (1963).
11. B. C. Stipe *et al.*, *Phys. Rev. Lett.* **87**, 277602 (2001).
12. T. R. Albrecht, P. Grutter, D. Horne, D. Rugar, *J. Appl. Phys.* **69**, 668 (1991).
13. G. P. Berman, D. I. Kamenev, V. I. Tsifrinovich, *Phys. Rev. A* **66**, 023405 (2002).
14. C. P. Slichter, *Principles of Magnetic Resonance* (Springer-Verlag, Heidelberg, ed. 3, 1996).
15. G. P. Berman, F. Borgonovi, H. S. Goan, S. A. Gurvitz, V. I. Tsifrinovich, *Phys. Rev. B* **67**, 094425 (2003).
16. T. A. Brun, H. S. Goan, *Phys. Rev. A* **68**, 032301 (2003).
17. H. Gassmann, M. S. Choi, H. Yi, C. Bruder, *Phys. Rev. B* **69**, 115419 (2004).
18. For measurement setups 1 and 2, we estimate the average magnitude of the lateral gradient to be $\sim 1.7 \times 10^5$ T m$^{-1}$.

19. Materials and methods are available as supporting material on *Science* Online.
20. We thank J. Sidles, K. Holczer, and A. Hero for discussions and D. Pearson and M. Sherwood for technical assistance. This work was supported by the Defense Advanced Research Projects Agency Three-Dimensional Atomic-Scale Imaging program administered through the U.S. Army Research Office.

**Supporting Online Material**
www.sciencemag.org/cgi/content/full/307/5708/408/DC1
Materials and Methods
Figs. S1 and S2
References

25 October 2004; accepted 15 December 2004
10.1126/science.1106718

# Slip-Rate Measurements on the Karakorum Fault May Imply Secular Variations in Fault Motion

**M.-L. Chevalier,[1,2] F. J. Ryerson,[2]* P. Tapponnier,[1] R. C. Finkel,[2] J. Van Der Woerd,[3] Li Haibing,[4] Liu Qing[5]**

**Beryllium-10 surface exposure dating of offset moraines on one branch of the Karakorum Fault west of the Gar basin yields a long-term (140- to 20-thousand-year) right-lateral slip rate of ~10.7 ± 0.7 millimeters per year. This rate is 10 times larger than that inferred from recent InSAR analyses (~1 ± 3 millimeters per year) that span ~8 years and sample all branches of the fault. The difference in slip-rate determinations suggests that large rate fluctuations may exist over centennial or millennial time scales. Such fluctuations would be consistent with mechanical coupling between the seismogenic, brittle-creep, and ductile shear sections of faults that reach deep into the crust.**

The Karakorum Fault in Tibet is the main Quaternary right-lateral fault north of the Himalayas. Determining its past and present motion is critical to understanding the kinematics of Asian continental deformation and the rheology of the continental lithosphere (*1*, *2*). The fault trends roughly parallel to the western Himalayan range, extending from at least Kailas to the Pamirs, a length of >1200 km (Fig. 1). Its Quaternary slip rate remains poorly constrained, compared to that of other large faults in Asia such as Kunlun, Haiyuan, and Altyn Tagh (*3*–*5*). Previous attempts to determine the rate have produced disparate values ranging from 1 to 30 mm/year (*2*, *6*–*11*). Such disparities may result from the different techniques applied and time periods observed, the part of the fault investigated, or its complex geometry, which displays multiple splays with oblique slip (*12*). We present measurements of the Mid- to Late Pleistocene slip rate on the southern stretch of the fault, based on $^{10}$Be surface exposure dating of two moraine crests displaced by the fault at the Manikala glacial valley terminus (32°2.529′N, 80°1.212′E, 4365 to 4760 m above sea level) (Figs. 1 and 2).

[1]Laboratoire de Tectonique, Mécanique de la Lithosphère, Unité Mixte de Recherche (UMR) 7578, CNRS, Institut de Physique du Globe de Paris, 75252 Paris Cedex 05, France. [2]Insitute of Geophysics and Planetary Physics, Lawrence Livermore National Laboratory, Livermore, CA 94550, USA. [3]Institut de Physique du Globe de Strasbourg, UMR 7516, CNRS, Strasbourg, France. [4]Laboratory of Continental Dynamics, Institute of Geology, Chinese Academy of Geological Sciences, Beijing 100037, China. [5]Total Exploration China, Total-Fina-Elf, Beijing, 100004, China.

*To whom correspondence should be addressed. E-mail: ryerson@llnl.gov

The Manikala moraine complex lies at the base of the faulted Ayilari range front, which bounds the west side of the Gar valley, a large pull-apart basin floored by marshland that hides other strands of the Karakorum Fault system (*13*) (Fig. 1). The moraines, M1 and M2, lie southeast of the U-shaped Manikala Valley, a glacial trough deeply entrenched into the range's igneous basement (Fig. 2 and fig. S1). The range front is marked by triangular facets as high as 800 m that testify to a normal component of slip on the fault. The principal strand of the fault shows discrete right-lateral offsets (10 ± 2 m, 35 ± 5 m, and 75 ± 5 m) of young rills of different depths, incised into postglacial colluvium (fig. S1). Within the till complex, two main groups of moraines are recognized (Fig. 2 and fig. S2). All were emplaced by the Manikala Daer glacier, whose terminus is today ~7 km upstream. The morphology of the moraines indicates that they correspond to major advances of the glacier and were later abandoned when the glacier retreated upstream (fig. S3).

The relative ages of the moraine groups can be qualitatively assessed from their surface characteristics (Fig. 2 and fig. S2). The M1 surface is rough and composed of chaotically distributed, imbricate blocks (as large as 3 m in diameter) surrounded by coarse debris. The smoother surface of M2 appears older, with blocks (tens of centimeters to a meter in diameter) protruding above a mantle of smaller debris (Fig. 2 and fig. S2). The morainic ridges thus appear to become younger from east to west, consistent with right-lateral motion on the fault.

The M2 moraine complex is divided into eastern and western sections (M2E and M2W, respectively) by a deep, beheaded, flat-floored paleovalley that is truncated by the fault and flanked by well-defined lateral moraines (Fig. 2). The crest of the lateral moraine east of the paleovalley is well preserved, and its eastern edge extends to the base of the faceted range front. There is no catchment on the mountain slope facing this valley, indicating that it must correspond to a former channel of the Manikala glacier (Fig. 2 and fig. S3). The youngest moraine group, M1 (Fig. 2), is the only one present on both sides of the Manikala outwash valley and displays well-preserved terminal lobes and sharply defined ridge crests.

Upstream from the fault, the limits of glacial incision reach the base of the triangular facets that border the Manikala valley. Downstream, the M1 and M2E moraine ridge crests extend linearly to the fault and, when realigned with the sharp edge of glacial bedrock incision south of the fault, provide the only piercing points accurate enough to obtain offset estimates (*14*) (Fig. 2 and fig. S4). Once restored from satellite images, the M1 and M2E offsets are 220 ± 10 m and 1520 ± 50 m, respectively. Another moraine complex with morphologically similar surfaces and offsets is found at the terminus of the Tajiang Daer glacial valley ~10 km to the west (fig. S3), lending additional support to this reconstruction (fig. S4).

$^{10}$Be model ages for samples collected along the moraine ridge crests (Fig. 2B) define consistent age clusters that can be used to date their abandonment (*15*). Ages on the two M2 ridges (Fig. 3) fall mostly between 103 and 204 thousand years (ky) (15 samples; mean age, 152 ± 28 ky), with a subset of seven samples between 132 and 150 ky old (mean age, 140 ± 5.5 ky). Samples WG-3, WG-4, and WG-7, on the eastern moraine (M2E), are more than 55 ky older than the main M2E population (132 to 150 ky old). We consider these three samples to be outliers, probably originating from more ancient till upstream. Examination of the M2 population with the outliers excluded reveals two distinct subgroups: a younger cluster of nine samples with ages of 103 to 149 ky (mean age, 133 ± 15 ky) and an older group of six samples of 160 to 204 ky (mean age, 181 ± 14 ky). The nine samples from the M1 moraine yield a younger mean age of 35 ± 9 ky. Seven samples fall between 36 and 45 ky (mean age, 40 ± 3 ky), and two distinctly younger samples have ages of 21 ± 1.0 ky.